Journal of Physics B: Atomic, Molecular and Optical Physics

PAPER • OPEN ACCESS

Effective temperatures in hot plasmas: the case of open-N-shell tin ions

To cite this article: J Sheil *et al* 2026 *J. Phys. B: At. Mol. Opt. Phys.* **59** 165004

IOP Publishing J. Phys. B: At. Mol. Opt. Phys. 59 (2026) 165004 https://doi.org/10.1088/1361-6455/ae9811

Journal of Physics B: Atomic, Molecular and Optical Physics

OPEN ACCESS

RECEIVED
17 March 2026

REVISED
10 July 2026

ACCEPTED FOR PUBLICATION
11 August 2026

PUBLISHED
24 August 2026

PAPER

Effective temperatures in hot plasmas: the case of open-N-shell tin ions

J Sheil[1,2,*], A J Neukirch[3], J Colgan[3] and Yu Ralchenko[4,5,6]

[1] Advanced Research Center for Nanolithography, Science Park 106, 1098 XG Amsterdam, The Netherlands
[2] Department of Physics and Astronomy, and LaserLaB, Vrije Universiteit, De Boelelaan 1100, 1081 HV Amsterdam, The Netherlands
[3] Los Alamos National Laboratory, Los Alamos, NM 87545, United States of America
[4] Department of Astronomy, University of Maryland, College Park, MD 20742, United States of America,
[5] X-Ray Astrophysics Laboratory, NASA Goddard Space Flight Center, Greenbelt, MD 20771, United States of America,
[6] CRESST-II, NASA Goddard Space Flight Center, Greenbelt, MD 20771, United States of America
[*] Author to whom any correspondence should be addressed.

E-mail: j.sheil@arcnl.nl

Keywords: collisional-radiative modeling, non-local thermodynamic equilibrium, EUV lithography, effective temperature

Abstract

Atomic populations in non-local thermodynamic equilibrium (non-LTE) plasmas often follow Boltzmann distributions at temperatures different from the electron temperature. We study the emergence of these so-called *effective temperatures* in open-N shell tin ions created in laser-produced plasmas relevant for extreme ultraviolet lithography. Configuration populations are calculated using the Los Alamos suite of atomic structure and population kinetics codes. We identify the collisional-radiative processes that dominate population transfer for hundreds of configurations in Sn^{11+}– Sn^{14+} ions in a range of plasma conditions. Our calculations reveal that the configuration populations are well-described by Boltzmann distributions at a single effective temperature. We attribute this behavior to the spontaneous emission process and the unique atomic structures of tin ions. We also show that a simple two-level model can reliably predict these effective temperatures.

1. Introduction

Accurate modeling of the radiative properties of hot plasmas requires detailed information on the structure and spectra of (typically) complex ions and knowledge of how these species interact with plasma electrons, photons, and ions. Consider, for example, the bound-bound contribution to the opacity of a medium κ_ν at photon frequency ν. This quantity, which governs radiation flow in plasma environments [1, 2], takes the form:

$$\kappa_\nu = \rho^{-1} \sum_{i<j} \sigma_\nu^{ij} \left[n_i - g_i g_j^{-1} n_j \right]. \tag{1}$$

Here, ρ is the mass density of the plasma, σ_ν^{ij} is the cross section for photoabsorption between energy levels i and j, g_i is the degeneracy of level i, n_i is its population density (simply 'population' in the following), and the sum runs over all levels (in all charge states ζ) separated by an energy $h\nu$. In the case of open-shell ions, this summation may have to include a huge number of levels (e.g. millions or more [3]) and billions of transitions [4] to obtain a reliable description of the radiative properties of the plasma.

Deriving the populations n_i involves calculating the rate at which population enters and leaves each level due to collisional and radiative processes in the plasma [5, 6]. This population flow is described mathematically by a system of collisional-radiative (CR) rate equations:

$$\frac{\mathrm{d}n_i}{\mathrm{d}t} = \sum_p \sum_{j \neq i} n_j \mathcal{R}_{ji}^p - n_i \sum_p \sum_{j \neq i} \mathcal{R}_{ij}^p. \tag{2}$$

Here, $\mathcal{R}_{ji}^{p}$ is the rate at which population is transferred from level j to level i due to a collisional or radiative process 'p'. Plasmas in which collisional processes dominate radiative ones are said to be in a state of local thermodynamic equilibrium (LTE). In LTE, the charge state populations are governed by the Saha equation, and the level populations are determined by the Boltzmann distribution $n_j/n_i = g_j \exp(-E_{ji}/k_B T_e)/g_i$, where $E_{ji} \equiv E_j - E_i$ is the energy difference between levels j and i, k_B is Boltzmann's constant, and T_e is the electron temperature (we omit k_B in equations that follow) [7]. Importantly, in LTE, one does not need to solve the CR rate equations to obtain the level populations; the Saha–Boltzmann (SB) relations suffice. This fact greatly simplifies the building of detailed, level-resolved LTE opacities for benchmarking purposes [8–13] as well as for stellar interior modeling [14–18]. For plasmas not in LTE, the more general 'non-LTE' situation, atomic populations are generally derived by solving equation (2).

The present study has multiple goals. The first is to evaluate, using equation (2), the populations of atomic configurations in open-N shell tin ions created in laser-produced plasmas (LPPs). Our primary interest in these plasmas stems from their use as extreme ultraviolet (EUV) radiation sources in computer chip manufacturing [19–21]. Opacities, emissivities and equation-of-state properties (collectively known as 'material' properties [22]) constitute basic input for radiation-hydrodynamic (rad-hydro) simulations of EUV light sources [23]. Improving the accuracy and completeness of tin material properties will undoubtedly increase the predictive capabilities of these simulations [23, 24]. The second goal of our study is to identify the CR processes that dominate population transfer between atomic configurations in these plasmas. The third goal of our study is to explain *why* our calculated non-LTE populations follow Boltzmann distributions at temperatures different from the electron temperature, at so-called *effective temperatures*. We show that a simple, two-level model gives very good predictions for these effective temperatures. Importantly, one can use these effective temperatures to generate (approximate) non-LTE material properties using LTE calculations.

2. non-LTE calculations

Before explaining the details of our calculations, we first describe the EUV radiation generated in laser-produced tin plasmas. Under optimal experimental conditions [25], the EUV spectrum consists of an intense emission feature centered near a wavelength of 13.5 nm [21, 26, 27]. In a recent paper [4], we conjectured that transitions from multiply-excited states of the form $4p^m4d^n4f^q - (4p^{m-1}4d^{n+1}4f^q + 4p^m4d^{n-1}4f^{q+1})$ in Sn^{11+}– Sn^{14+} ions are largely responsible for this radiation. Taking Sn^{12+} as an example, we have $m+n+q=8$ and the transition array $4p^64d4f - (4p^54d^24f + 4p^64f^2)$ originates from two such *doubly excited* configurations [28]. While recent theoretical works support our hypothesis [29–32], its confirmation will ultimately rely on charge-state resolved measurements of transitions from multiply-excited states [33]. This remains an open challenge in tin-ion spectroscopy.

From an atomic structure perspective, the combination of open $4p, 4d$ and $4f$ subshells generates a huge number of energy levels, so large that one cannot solve equation (2) to obtain level populations even with modern CR codes [3]. That said, level-resolved calculations are essential for deriving accurate spectra given the presence of strong configuration-interaction effects in these systems [34–37]. It is these competing aspects of tractability and accuracy that makes challenging the accurate calculation of tin opacities.

Our approach to this problem, presented in [2] and submitted to the EUV Light Sources Code Comparison Workshop [38], is to exploit the concept of *effective temperatures* in non-LTE plasmas [7, 39–44]. In plasmas with Maxwellian-distributed free electrons, it is very often the case that populations derived from equation (2) follow Boltzmann distributions at temperatures different from the electron temperature T_e. These temperatures are generally known as *effective temperatures*. Their emergence can be traced to the spontaneous emission process, whose non-negligible role in non-LTE plasmas essentially modifies the Boltzmann distribution from one at T_e (LTE conditions) to one at T_{eff} (non-LTE conditions) [44]. In 1993, Busquet [45] described a method for approximating level-resolved, non-LTE opacity spectra using effective temperatures. The method involves identifying a so-called 'ionization temperature' T_{eff} for which an LTE calculation reproduces the average charge state $\langle Z\rangle$ of a non-LTE calculation performed at T_e. Assuming that the non-LTE populations are well-described by a Boltzmann distribution at T_{eff}, one then approximates a non-LTE opacity at T_e using an LTE opacity calculation at T_{eff}. We adopted this approach in [2] to derive opacity spectra for Sn^{12+} and Sn^{14+} ions in two sets of plasma conditions: $\rho = 2\times10^{-4}$ g cm^{-3} with (i) $T_e = 36$ eV and (ii) $T_e = 33$ eV and a Planckian radiation field with radiation temperature $T_r = 21$ eV. The present work extends our investigation of effective temperatures to (i) more ions and (ii) a wider range of plasma conditions.

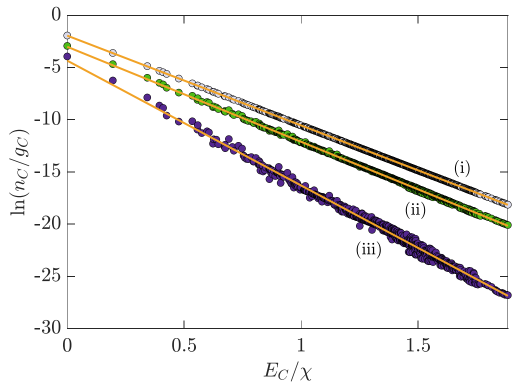

Figure 1. Reduced configuration populations $\ln(n_C/g_C)$ as a function of E_C/χ for Sn^{14+}. Our calculations give $\chi = 383.8$ eV. The plasma conditions are $T_e = 45$ eV and $\rho = 2 \times 10^x$ g cm^{-3} where $x =$ (i) -2 (light purple), (ii) -3 (green) and (iii) -4 (dark purple). The case numbers, i.e., (i), (ii) and (iii) are indicated in the plot. Yellow solid lines show first-order polynomial fits to the reduced configuration populations. To improve the readability of the plot (specifically; to avoid dataset crossings), the reduced configuration populations in cases (i) and (ii) have been multiplied by factors of 125 and 25, respectively. Care must therefore be taken in interpreting the populations shown in this plot.

The calculations presented in the current work follow those described in [2]. We calculate non-LTE populations using the Los Alamos CATS [46, 47] and ATOMIC [48, 49] codes in configuration-average (CA) mode. In the CA mode, levels are grouped into configurations, configuration-to-configuration rates $\mathcal{R}^p_{C'C} = \sum_{j\in C'}\sum_{i\in C} g_j g_{C'}^{-1}\mathcal{R}^p_{ji}$ are derived ($g_{C'} \equiv \sum_{j\in C'} g_j$ is the total statistical weight of configuration C'), and a CR rate equation is solved for each configuration [7]. Our atomic model includes (i) all single-electron excitations from principal quantum number $n = 4$ to $n = 10$, (ii) double excitations from $n = 4$ to $n = 5$, and (iii) a limited number of trebly excited configurations (see table 1 in [2] for a list of configurations). The atomic model for Sn^{14+}, for example, includes 714 configurations with $\sum_C g_C = 4.798 \times 10^6$. The following atomic processes are included in the calculations: spontaneous emission (*se*), electron-impact excitation (*ce*), electron-impact de-excitation (*de*), electron-impact ionization (*ci*), three-body recombination (*tbr*), radiative recombination (*rr*), autoionization (*ai*) and dielectronic capture (*dc*). Cross-sections for *ce* are calculated using the plane-wave Born approximation implemented in the CATS code, and *ci* cross-sections are calculated using the GIPPER code [50]. We do not consider the photon-driven processes of photoabsorption, photoionization, stimulated emission or stimulated recombination. As such, there are no inverse processes associated with the spontaneous emission or radiative recombination processes; they are *unbalanced* processes. As will soon be made clear, it is this unbalanced aspect from which effective temperatures emerge. Inspired by the case studies at the EUV Light Sources Code Comparison Workshop [38], we choose mass densities in the range $\rho = 2 \times 10^x$ g cm^{-3} with $x = -2, -3$ and -4 and electron temperatures $T_e = 30$ and 45 eV. The calculations presented in this work do not include the effects of continuum lowering on the atomic structure. This decision was based on an additional CR calculation we performed that included continuum lowering (implemented via the Stewart–Pyatt formalism [51]) for the highest density case, where we found that the average charge state changed by as little as 0.5.

3. Results

3.1. Reduced configuration populations

In figure 1 we present plots of the logarithm of the 'reduced configuration populations', $\ln(n_C/g_C)$, as a function of the ionization potential (χ)-normalized configuration-average energy E_C/χ for Sn^{14+}. Our calculations give $\chi = 383.8$ eV. The plasma conditions are $T_e = 45$ eV and $\rho = 2 \times 10^x$ g cm^{-3} for $x =$ (i) -2 (light purple), (ii) -3 (green), and (iii) -4 (dark purple). The case numbers, i.e., (i), (ii) and (iii), are indicated in the plot. We define T_{eff} as the product of χ with the negative-inverse of the slope of the line of best-fit through the reduced configuration populations. The solid yellow lines represent first-order polynomial fits to the reduced configuration populations. Denoting the free-electron density by n_e and the fractional population of Sn^{14+} ions by P^{14+}_{frac}, the plasma conditions give [n_e (cm^{-3}), $\langle Z\rangle, P^{14+}_{\text{frac}}$] $\approx$ (i) $[1.3 \times 10^{21}, 12.8, 0.19]$, (ii) $[1.5 \times 10^{20}, 14.9, 0.25]$ and (iii) $[1.4 \times 10^{19}, 14.2, 0.43]$. To improve the readability of the plot (specifically; to avoid dataset crossings), the populations in cases (i) and (ii) have been multiplied by factors of 125 and 25, respectively.

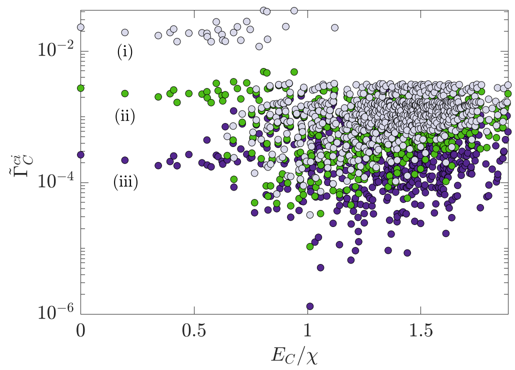

Figure 2. Fractional contribution of collisional ionization to population outflux, $\tilde{\Gamma}_C^{ci}$, for Sn^{14+}. The plasma conditions, cases and color scheme are the same as that shown in figure 1.

The key take-away from figure 1 is the near-linear dependence of $\ln(n_C/g_C)$ on E_C/χ in all three cases. Linearity is especially strong in case (i), where we find that $T_{\rm eff} = 44.6$ eV $\approx T_{\rm e}$; the plasma is thus close to LTE conditions. While the deviation between the configuration populations and the line of best-fit through them increases with decreasing density (the plasma becomes 'more non-LTE'), the accuracy of the fits remain very good. We find that $T_{\rm eff} \approx 42$ and 32 eV in cases (ii) and (iii), respectively. Even in the strongly non-LTE conditions associated with case (iii), a single effective temperature works well in describing the population distribution across the entire ion. This single-temperature description however starts to break down for free-electron densities below $n_{\rm e} = 10^{19}$ cm^{-3}. CR calculations we have performed at free-electron densities of $n_{\rm e} = 10^{17}$ and 10^{18} cm^{-3} reveal groups of configurations following their own temperature law. It is very likely that these represent the so-called 'superconfiguration temperatures' studied in [7, 44]. Work is in progress to better understand the emergence of these temperatures at low $n_{\rm e}$ values. One goal of the present paper is to understand *why* a single effective temperature works so well in describing the configuration population distributions in the present cases. We also investigate the following questions:

1. What CR processes dominate population transfer between configurations?
2. What radiative channels are responsible for the emergence of effective temperatures?
3. Why does a single effective temperature work so well in describing the reduced configuration population distributions?
4. Can we predict $T_{\rm eff}$ a priori, that is without solving equation (2) and performing fits to the reduced configuration populations?

3.2. CR processes

Our answer to the first question above starts with an analysis of the CR processes that act to *depopulate* each configuration. In the following, we let $\Gamma_C^p \equiv n_C \sum_{C'} \mathcal{R}_{CC'}^p$ denote the population *outflux* from configuration C arising from one of the six processes $\{se, ce, de, ci, ai, dc\}$. Furthermore, let $\tilde{\Gamma}_C^p$ denote the *fractional contribution* of process p to population outflux:

$$\tilde{\Gamma}_C^p \equiv \frac{\Gamma_C^p}{\Gamma_C^{se} + \Gamma_C^{ce} + \Gamma_C^{de} + \Gamma_C^{ci} + \Gamma_C^{ai} + \Gamma_C^{dc}}. \tag{3}$$

From its definition, $\tilde{\Gamma}_C^p$ is independent of n_C and is normalized according to $\sum_p \tilde{\Gamma}_C^p = 1$. Let us now look at some examples. In figure 2 we plot the fractional contribution of collisional ionization to population outflux, $\tilde{\Gamma}_C^{ci}$, for each configuration in Sn^{14+} for cases (i), (ii) and (iii) (we adopt the same color scheme as in figure 1. Case numbers are again indicated in the plot). Be it either from bound ($E_C/\chi < 1$) or autoionizing configurations ($E_C/\chi \geqslant 1$), collisional ionization plays a negligible role. Essentially, the large ionization potential of Sn^{14+} (383.8 eV) means that collisional ionization from low-lying configurations can only be mediated by electrons with kinetic energies much greater than $T_{\rm e}$. However, these electrons have a relatively low population in these plasmas. Collisional ionization from autoionizing configurations is simply dwarfed by autoionization and collisional excitation and de-excitation processes (see below).

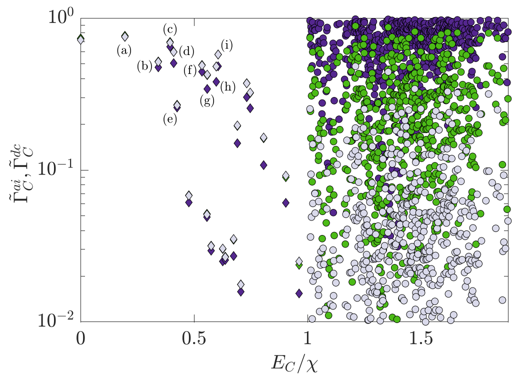

Figure 3. Same as figure 2 but for $\tilde{\Gamma}_C^{ai}$ and $\tilde{\Gamma}_C^{dc}$. The labels represent the following configurations: (a) $4p^54d$, (b) $4s4p^64d$, (c) $4p^44d^2$, (d) $4p^54f$, (e) $4p^55s$, (f) $4s4p^54d^2$, (g) $4s4p^64f$, (h) $4p^34d^3$ and (i) $4p^44d4f$. Diamonds represent the fractional contribution of dielectronic capture to population outflux, and circles represent the fractional contribution of autoionization to population outflux.

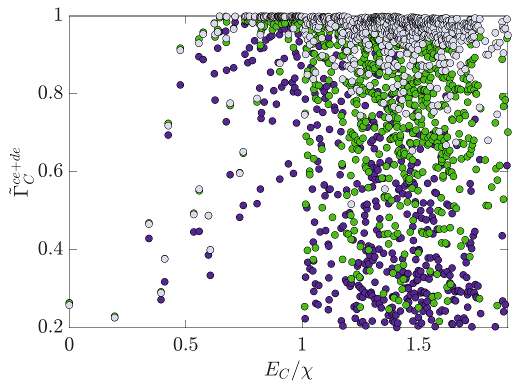

Figure 4. Same as figure 2 but for $\tilde{\Gamma}_C^{ce+de}$.

The autoionization process is only relevant for configurations with $E_C/\chi \geqslant 1$. We present in figure 3 the fractional contribution of autoionization to population outflux, $\tilde{\Gamma}_C^{ai}$. This is the dominant ionization channel for most configurations in case (iii). The situation is more complicated for cases (i) and (ii), as here collisional excitation and de-excitation processes become increasingly relevant with increasing density (this can be confirmed by examining the quantity $\tilde{\Gamma}_C^{ce+de} \equiv \tilde{\Gamma}_C^{ce} + \tilde{\Gamma}_C^{de}$ presented in figure 4). Only two configurations in case (i), for instance, have $\tilde{\Gamma}_C^{ai} > 0.5$. While configurations with $E_C/\chi < 1$ cannot autoionize, they can lose population via the dielectronic capture (*dc*) mechanism (the inverse process of autoionization). Levels associated with the doubly excited $4p^54d4f$ configuration in Sn^{13+} can, for instance, be populated via *dc* from the $4p^6\,{}^1S_0$ level of Sn^{14+}. The diamonds in figure 3 represent the fractional contribution of *dc* to population outflux, $\tilde{\Gamma}_C^{dc}$. This is the dominant outflux channel for the ground-state configuration as well as a number of excited configurations labeled in the figure: (a) $4p^54d$, (b) $4s4p^64d$, (c) $4p^44d^2$, (d) $4p^54f$, (e) $4p^55s$, (f) $4s4p^54d^2$, (g) $4s4p^64f$, (h) $4p^34d^3$ and (i) $4p^44d4f$. In terms of the ground and $4p^54d$ configurations, $\tilde{\Gamma}_C^{dc}$ exhibits a very weak dependence on density in all three cases. While this is also true for configurations (b) - (i) in cases (i) and (ii), a noticeable reduction in $\tilde{\Gamma}_C^{dc}$ occurs for case (iii). At these low densities, the CA spontaneous emission rate becomes comparable to rates associated with collisional processes; see figure 5 below. From figure 3 we also learn that *dc* is *not* the dominant outflux mechanism for most configurations with $0.5 < E_C/\chi < 1$.

We are now left with three processes to examine: spontaneous emission, collisional excitation, and collisional de-excitation. The latter two processes are, of course, inverses of each other, and our omitting an external radiation field in the calculations makes the *se* process an *unbalanced* one. It is precisely this unbalanced aspect from which effective temperatures emerge, for if we were to pump the plasma with a Planckian radiation field at $T_r = T_e$, then it would be in a state of full thermodynamic equilibrium. In figure 5 we present the fractional contribution of spontaneous emission to population outflux, $\tilde{\Gamma}_C^{se}$. Notice the exceedingly large spread of $\tilde{\Gamma}_C^{se}$ values in each case: some close-lying configurations differ in $\tilde{\Gamma}_C^{se}$ value by more than an order-of-magnitude.

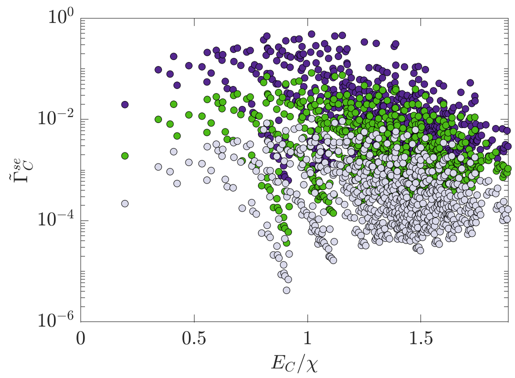

Figure 5. Same as figure 2 but for $\tilde{\Gamma}_C^{se}$.

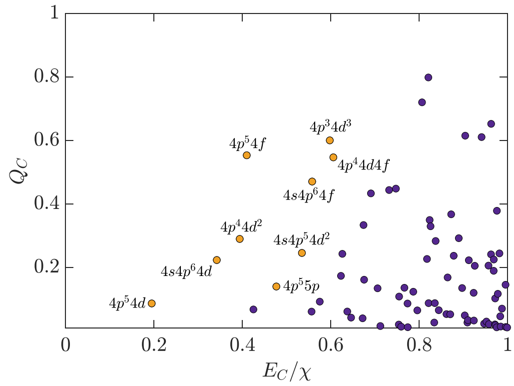

Figure 6. Quenching parameter $Q_C \equiv \tilde{\Gamma}_C^{se}/\tilde{\Gamma}_C^{ce+de}$ as a function of E_C/χ for Sn^{14+} in case (iii). The yellow-filled circles have their configuration labeled beside them.

The contribution of spontaneous emission to population outflux in cases (i) and (ii) is relatively small: the maximum values of $\tilde{\Gamma}_C^{se}$ lie below 0.01 and 0.1, respectively. It must therefore be that collisional excitation and de-excitation processes dominate population outflux for most configurations with $0.5 < E/\chi < 1$ in these cases. This can be confirmed by again examining figure 4. Another important aspect of figure 5 is the near-uniform, order-of-magnitude increase in $\tilde{\Gamma}_C^{se}$ comparing cases (i) and (ii). This trend continues to case (iii) with the important caveat that the spontaneous emission rates are now comparable to (if not greater than) the rates for collisional excitation and de-excitation.

The above paragraphs provide a detailed answer to the question of what CR processes dominate population transfer between configurations. Similar conclusions can be drawn for Sn^{11+}– Sn^{13+} ions (see figures 7–15 in the appendix).

3.3. Radiative channels

Our answer to the question of what radiative channels are responsible for the emergence of effective temperatures starts with the definition of a new quantity $Q_C \equiv \tilde{\Gamma}_C^{se}/\tilde{\Gamma}_C^{ce+de}$. We call this quantity the 'quenching parameter'; it simply tells us how important the spontaneous emission process is compared to collisional excitation and de-excitation processes. We present this quantity in figure 6 for case (iii), where we have labeled nine low-lying configurations with large Q_C values (yellow circles). In the following paragraph, we examine the various channels through which the levels associated with these configurations can decay.

Not much needs to be said about the lowest-lying excited configuration $4p^54d$. Its $^1P_1$ level [52] undergoes a strong electric-dipole (E1) transition to the $4p^6\,^1S_0$ level. Levels associated with the next highest-lying configuration in the figure, $4s4p^64d$, can decay to levels of the aforementioned $4p^54d$ configuration through $4s-4p$ transitions. Moving to higher excitation energies we encounter the two close-lying configurations $4p^44d^2$ and $4p^54f$. Again, certain levels admit strong E1 transitions to levels of the aforementioned $4p^54d$ configuration. Given their close proximity in energy, strong mixing between their levels will occur in a CI calculation, and transitions from these configurations are best described as a mixed $4p^54d-(4p^44d^2+4p^54f)$ array. Configurations formed by imposing a vacancy in the $4s$ subshell of these excited configurations, $4s4p^54d^2$ and $4s4p^64f$, also admit large Q_C values. These levels can decay to levels of the $4s4p^64d$ configuration. Moving to even higher excitation energies we encounter the trebly excited $4p^34d^3$ and doubly excited $4p^44d4f$ configurations. Again, we expect their levels to undergo strong mixing in a CI calculation, and that the dominant decay pathway is to levels of the $4p^44d^2$ configuration.

The radiative channels described above are ultimately responsible for the emergence of effective temperatures in these plasmas. They all involve $\Delta n=0$ transitions of the form $4s-4p$, $4p-4d$ or $4d-4f$. Importantly, the excited configurations $4p^{m-1}4d^{n+1}4f^q$ and $4p^m4d^{n-1}4f^{q+1}$ have very similar CA energies. What is more, the energy difference between upper and lower configurations is near-independent of excitation order. For example,

$$E_{4p^54d}-E_{4p^6}\approx E_{4p^44d^2}-E_{4p^54d}\approx E_{4p^34d^3}-E_{4p^44d^2}\approx 75\ \text{eV}.$$

This observation will play an important role in the following section where we explain why a single effective temperature works so well in describing the configuration population distributions. However, before proceeding there we answer one final question: are the radiative channels shown in figure 6 also relevant for other charge states? The answer, at least for Sn^{11+}– Sn^{13+} ions, is yes (see figures 7–9 and figures 12–17 in the appendix). We now have a complete answer to the question of what radiative channels are responsible for the emergence of effective temperatures.

3.4. Effective temperatures

We now return to the topic of effective temperatures. We wish to answer two questions: (i) why does a single effective temperature work so well in describing the reduced configuration population distributions shown in figure 1?, and (ii) is it possible to predict T_{eff} analytically, that is, without resorting to fits of the reduced configuration populations derived from the solution of equation (2)?

The works of Bowen [53], Busquet [42], and Hansen *et al* [43] investigated ways to make analytic predictions for T_{eff}. The method adopted in those studies is to reduce the multi-level (or multi-configuration) kinetics description to a two-level one, either between the ground levels of adjacent charge states [53] or to levels in the same ion [42, 43].

Here we describe the second approach, where population flow between the two levels (labeled '1' and '2' in the following) is driven by collisional excitation, collisional de-excitation, and spontaneous emission. Using van Regemorter's formula for the collisional de-excitation cross section [54], the collisional de-excitation rate takes the form $\mathcal{R}_{21}^{de}=1.6\times10^{-5}n_ef_{21}\bar{g}E_{21}^{-1}T_e^{-1/2}$ [53] (E_{21} is in eV), where E_{21} is the energy separation between the levels, f_{21} is the oscillator strength for the transition and $\bar{g}$ is the effective Gaunt factor for the transition. Using the principle of detailed balance [7] to write $\mathcal{R}_{12}^{ce}$ in terms of $\mathcal{R}_{21}^{de}$, and taking $\mathcal{R}_{21}^{se}=4.3\times10^7f_{21}E_{21}^2$ [53], we derive the following formula for the ratio of the populations of the upper and lower levels:

$$\frac{n_2}{n_1}=\frac{g_2}{g_1}\exp\left(\frac{-E_{21}}{T_e}\right)\left[1+\frac{\mathcal{C}E_{21}^3T_e^{1/2}}{n_e\bar{g}}\right]^{-1}. \tag{4}$$

The second term inside the square bracket is the ratio of the spontaneous emission rate to the collisional de-excitation rate $\mathcal{R}_{21}^{se}/\mathcal{R}_{21}^{de}$, from which the constant $\mathcal{C}=2.69\times10^{12}\ \text{eV}^{-7/2}\ \text{cm}^{-3}$ emerges. Equation (4) naturally recovers the Boltzmann distribution in the high density, low-temperature limit, i.e., in LTE conditions. Supposing that the ratio of the reduced populations is governed by an effective temperature T_{eff}^*, that is $(n_2g_2^{-1})/(n_1g_1^{-1})=\exp(-E_{21}/T_{\text{eff}}^*)=\exp(-E_{21}/T_e)(1+\mathcal{C}E_{21}^3T_e^{1/2}/(n_e\bar{g}))^{-1}$, one can write the effective temperature in the following form:

$$\frac{1}{T_{\text{eff}}^*}=\frac{1}{T_e}+\frac{1}{E_{21}}\ln\left[1+\frac{\mathcal{C}E_{21}^3T_e^{1/2}}{n_e\bar{g}}\right]. \tag{5}$$

This equation tells us that T_{eff}^* is always less than T_e, and that the spontaneous emission processes is responsible for the emergence of effective temperatures in the two-level model. This is also true for multi-level/configuration/superconfiguration population kinetics models [44].

We now check if equation (5) provides accurate predictions for T_{eff} in the cases studied in the present work. To do this, we must treat configurations as single energy levels. We first consider population flow between the $4p^6$ and $4p^54d$ configurations in Sn^{14+}. In case (iii), these two configurations accumulate approximately 95% of the total ion population. Taking $E_{21}=E_{4p^54d,4p^6}\approx75$ eV, and

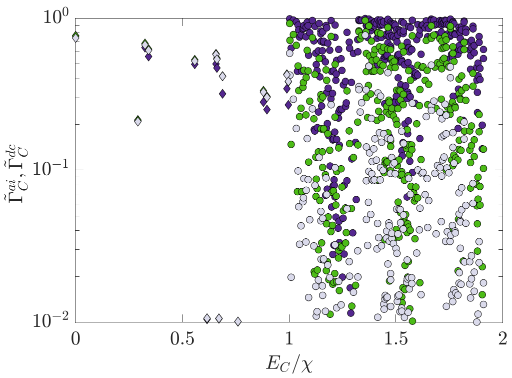

Figure 7. Same as figure 3 but for Sn^{11+}. Our calculations give $\chi = 231.3$ eV.

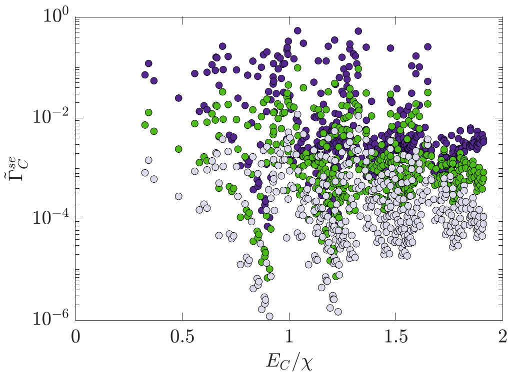

Figure 8. Same as figure 5 but for Sn^{11+}.

$\bar{g} = 0.6 + 0.28\ln[1 + (0.562 + 1.4\mathcal{F})/(\mathcal{F} + 1.4\mathcal{F}^2)] \approx 0.72$, ($\mathcal{F} \equiv E_{21}/T_e$) [43, 55, 56] (this form for $\bar{g}$ is appropriate for $\Delta n = 0$ transitions), we find $T^*_{\text{eff}} = 31.4$ eV. This is quite close to a value of 32.5 eV obtained from the slope of the line drawn between the reduced configuration populations for these two configurations (recall that $T_{\text{eff}} = 32.1$ is obtained for the entire ion). Choosing $\bar{g} = 0.8$, slightly larger than that given by the formula above, brings T^*_{eff} and T_e into excellent agreement with each other. Possible reasons why the two-level model works so well for Sn^{14+} are that (i) the lower configuration only has one level ($^1S_0$) and (ii) almost all of the oscillator strength is concentrated in the $^1S_0 - ^1P_1$ transition [52]. Thus, our 'approximating' the upper configuration as a single level is perhaps not too erroneous.

We are now in a position to explain *why* a single effective temperature works so well in describing the reduced configuration population distributions. The reason lies in the fact that the relevant radiative channels involve $\Delta n = 0$ transitions where the energy separation between adjacent excitation orders is nearly constant. To demonstrate this, consider again the two-level model with the lower 'level' being $4p^5 4d$ (previously the upper level) and the upper level being either $4p^4 4d^2$ or $4p^5 4f$. Taking $\bar{g} = 0.8$ and $E_{21} = E_{4p^4 4d^2, 4p^5 4d} \approx 75$ eV gives $T^*_{\text{eff}} \approx T_{\text{eff}}$ (taking $E_{21} = E_{4p^5 4f, 4p^5 4d} \approx 83$ eV gives $T^*_{\text{eff}} \approx 31$ eV). Extending the two-level model to the even higher-lying $4p^3 4d^3$ and $4p^4 4d 4f$ configurations will give $T^*_{\text{eff}} \approx T_{\text{eff}}$. Thus, it is regularities in the atomic structure that promote the emergence of a single effective temperature governing the reduced configuration population distributions. We will study the situation for even lower free-electron densities in a future work.

We will now go a step further and investigate the situation for charge states other than Sn^{14+}. In figures 7–9 we present the quantities $\tilde{\Gamma}_C^{ai}, \tilde{\Gamma}_C^{dc}, \tilde{\Gamma}_C^{se}$ and Q_C for Sn^{11+}, whose ground state configuration takes the form $4p^6 4d^3$. Importantly, many of the conclusions we have already drawn for Sn^{14+} are applicable to Sn^{11+}. This is also true for the Sn^{12+} and Sn^{13+} ions (see figures 12–17 in the appendix). These ions are more complex than Sn^{14+} due to their open-$4d$ subshell ground-state configurations. The ions Sn^{15+} and Sn^{16+} are also more complex than Sn^{14+} given their open $4p$-subshell ground-state configurations. Thus, the ions adjacent to Sn^{14+} are an excellent testing ground for the applicability of the two-level model.

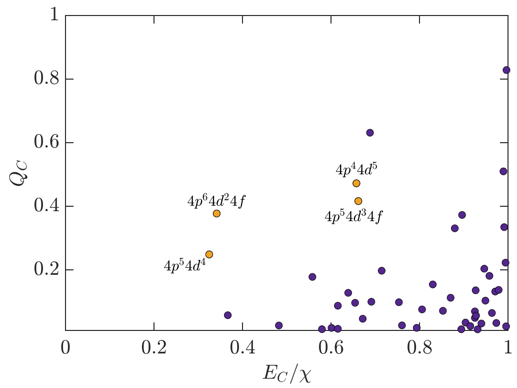

Figure 9. Same as figure 6 but for Sn^{11+}. Our calculations give $\chi = 231.3$ eV.

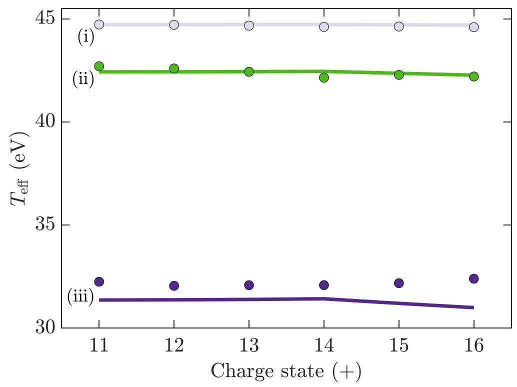

Figure 10. Circles represent effective temperatures derived from fits to the reduced configuration populations for charge states Sn^{11+}– Sn^{16+}. The plasma conditions correspond to $T_e = 45$ eV and $\rho = 2 \times 10^x$ g cm^{-3} with $x =$ (i) -2 (light purple circles), (ii) -3 (green circles), and (iv) -4 (dark purple circles). The solid lines correspond to the predictions of equation (5) with $E_{21} = E_{4p^54d^{n-1},4p^64d^n}$ for Sn^{11+}– Sn^{13+} ions and $E_{21} = E_{4p^{m-1}4d,4p^m}$ for Sn^{14+}– Sn^{16+} ions.

We have derived effective temperatures for Sn^{11+}– Sn^{16+} ions for cases (i), (ii) and (iii). As in the Sn^{14+} case, we find that a single effective temperature very well describes the reduced configuration population distributions. Effective temperatures derived from fits to the reduced configuration populations are shown as circles in figure 10. Solid lines are the predictions of equation (5), where we have taken $E_{21} = E_{4p^54d^{n-1},4p^64d^n}$ for Sn^{11+}– Sn^{13+} ions and $E_{21} = E_{4p^{m-1}4d,4p^m}$ for Sn^{14+}– Sn^{16+} ions. These energies were also used to derive charge state-specific $\bar{g}$ values. It is clear from figure 10 that the two-level model gives very accurate predictions for $T_{\rm eff}$ for all charge states in cases (i) and (ii). The agreement worsens for case (iii), which is likely due to the growing non-LTE nature of the plasma with decreasing n_e. This disagreement can be remedied by using a constant value of $\bar{g} = 0.8$ for the Gaunt factor for all ions.

To test the applicability of the two-level model closer to LTE conditions, we performed a second set of calculations where we lowered the electron temperature to $T_e = 30$ eV. The results, presented in figure 11, clearly show that the two-level model gives excellent predictions for $T_{\rm eff}$ for all charge states in all three cases. Using a constant value of $\bar{g} = 0.8$ overestimates the effective temperature by approximately 1 eV for all ions in case (iii).

To conclude the above discussion, we have found that (i) the effective temperatures are near-independent of charge state, and (ii) they can be predicted with very good accuracy using equation (5). One can use this information to approximate non-LTE material properties using LTE computations. This approach would overcome many of the limitations associated with using inline, highly simplified non-LTE models in rad-hydro simulations [22].

4. Future work

All of the calculations presented in this work were performed for optically thin plasmas; that is, we do not consider the photon-driven processes of photoabsorption, photoionization, stimulated emission

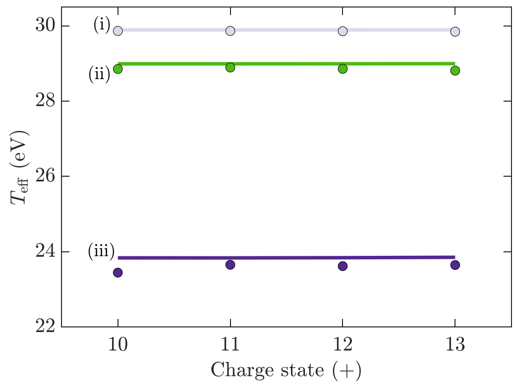

Figure 11. Same as figure 10 but for $T_e = 30$ eV and for $Sn^{10+} - Sn^{13+}$ ions.

or stimulated recombination in our model. Accounting for photoabsorption and photoionization processes in a CR model requires knowing (i) the radiation field driving these processes and (ii) their cross sections. Photoabsorption cross sections are proportional to the absorption oscillator strength of the transition, which, for Sn ions, are strongest in the aforementioned narrow wavelength interval around 13.5 nm ($\sim$92 eV). Photoabsorption rates, which are found by integrating the photoabsorption cross section over the photon energy-normalized, angular-averaged radiation field, are very likely dominated by photons in this narrow wavelength interval.

Our previous work [2] found that pumping a $T_e = 33$ eV plasma with a $T_r = 21$ eV Planckian radiation field did not spoil the emergence of an effective temperature (we found $T_{\mathrm{eff}} \approx 27$ eV). Even for this Planckian radiation field, it is very likely that only photons in the narrow wavelength interval around 13.5 nm make a significant contribution to photoabsorption rates. Because the radiation field inside an EUV source is dominated by intense emission in this wavelength interval, we believe that effective temperatures will also emerge in plasmas driven by 'realistic' radiation fields. Work is in progress to confirm this hypothesis. Other means of studying photon-driven processes could include (i) introducing a radiation field into the two-level model (which would introduce the processes of photoabsorption and stimulated emission) or (ii) reducing the spontaneous emission rate, an approach sometimes taken in zero-dimensional kinetics codes to emulate the effects of optical depth through so-called 'escape factors' [57, 58].

Another very promising approach for generating radiation-field-dependent non-LTE material properties is the linear response method (LRM) [22]. Its primary application to-date has been to generate material property data for simulations of high-temperature, strongly non-LTE gold hohlraum plasmas [22, 59].The basic idea of the LRM is as follows. First, one generates material properties using a limited set of 'reference' radiation fields relevant for the application, e.g., for the inertial confinement fusion hohlraum simulations presented in [22], Planckian radiation fields (as well as ones modified to contain additional radiation in the $2-3$ keV photon range) were employed. In the following, we call the material properties generated with these reference radiation fields 'reference material properties'. In the second step of the LRM, one perturbs the radiation field at each photon frequency, recalculates the material properties using this radiation field, and constructs derivatives of the material properties with respect to the radiation field at each photon frequency. With all of this information, one can construct material properties for an arbitrary radiation field by Taylor expanding the reference material properties (the aforementioned derivatives appear in this Taylor expansion). The tabulated nature of the LRM allows for using detailed, non-LTE material properties in rad-hydro simulations that cannot be provided by inline atomic models. Howard A. Scott was the first to apply the LRM to tin LPP conditions [60]. We intend to continue this line of research in the future.

Finally, one can ask whether the notion of effective temperatures extends to even shorter-wavelength light source plasmas, such as gadolinium or bismuth plasmas of interest to beyond-EUV lithography near 6.7 nm [61] and biological imaging in the water window region (2.3–4.4 nm) [62], respectively. The charge states responsible for emission at these wavelengths are higher than the 13.5 nm-emitting tin ions; ions in the neighborhood of Pd-like Gd^{18+} and Bi^{37+} are relevant [63, 64]. Synthesizing these ions in plasmas with free-electron densities similar to the tin case necessitates even higher electron temperatures. If effective temperatures do exist in these systems, we expect them to be substantially smaller than T_e. Let us estimate the effective temperature for a gadolinium plasma using equation (5). Taking

$T_e = 110$ eV [65], $E_{21} = 183$ eV (the energy separation between the $4d^{10}\,{}^1S_0$ and $4d^9 4f\,{}^1P_1$ levels in Gd^{18+}[66, 67]), $n_e = 10^{19}$ cm^{-3} and $\bar{g} = 0.8$, we have $T^*_{\mathrm{eff}} \approx 38$ eV, nearly a factor of three smaller than T_e. Proof of the existence (or absence) of effective temperatures will, however, ultimately rely on solving the system of CR rate equations.

5. Conclusions

We have presented a comprehensive study of configuration population distributions and CR processes in tin plasmas relevant for EUV lithography. Calculations were performed with the Los Alamos CATS and ATOMIC codes. It was found that the configuration populations follow Boltzmann distributions at temperatures different to the electron temperature. We attribute the emergence of these effective temperatures to the unbalanced spontaneous emission process, whose importance grows with decreasing free-electron density. It was found that a simple, two-level model gives accurate predictions for the effective temperatures. We attribute this to two facts: (i) the dominant radiative channels are all $\Delta n = 0$ transitions and (ii) the transition energy is near-independent of excitation order. Avenues for future work were also presented.

Acknowledgements

This paper is dedicated to the memory of our friend and collaborator Howard A. Scott. J. Sheil would like to thank S. B. Hansen for informing him of the form of the Gaunt factor used in this work. Part of this work was completed while J. Sheil was a visitor at Los Alamos National Laboratory; he would like to thank the Theory Division for their kindness and hospitality during his stay. We thank I. E. Golovkin, A. Sasaki, V. Bakshi, and O. O. Versolato for useful discussions. This publication is part of the project ARIES with file number 20152 of the research programme VENI which is (partly) financed by the Dutch Research Council (NWO). Part of this work was conducted at the Advanced Research Center for Nanolithography, a public-private partnership between the University of Amsterdam, Vrije Universiteit Amsterdam, University of Groningen, the Netherlands Organization for Scientific Research (NWO), and the semiconductor equipment manufacturer ASML. The work of Y.R. was supported by NASA under award number 80GSFC24M0006. Part of this work was supported by the ASC PEM program of the US Department of Energy through the Los Alamos National Laboratory. Los Alamos National Laboratory is operated by Triad National Security, LLC, for the National Nuclear Security Administration of U.S. Department of Energy (Contract No. 89233218CNA000001).

Data availability statement

The data that support the findings of this study are available upon reasonable request from the authors.

Author contributions

J Sheil 0000-0003-3393-9658
Conceptualization (lead), Formal analysis (lead), Funding acquisition (equal), Investigation (lead), Methodology (equal), Project administration (lead), Software (equal), Validation (lead), Visualization (lead), Writing – original draft (lead), Writing – review & editing (equal)

A J Neukirch 0000-0002-6583-0086
Conceptualization (equal), Data curation (lead), Formal analysis (equal), Funding acquisition (equal), Investigation (equal), Methodology (equal), Resources (lead), Software (lead), Writing – review & editing (equal)

J Colgan 0000-0003-1045-3858
Conceptualization (equal), Data curation (lead), Formal analysis (equal), Funding acquisition (equal), Investigation (equal), Methodology (equal), Resources (lead), Software (lead), Writing – review & editing (equal)

Yu Ralchenko 0000-0003-0083-9554
Data curation (equal), Formal analysis (equal), Funding acquisition (equal), Investigation (equal), Methodology (equal), Resources (lead), Software (lead), Writing – review & editing (equal)

Appendix

The first part of this appendix contains plots of $\tilde{\Gamma}_C^{ai}$, $\tilde{\Gamma}_C^{dc}$, and $\tilde{\Gamma}_C^{se}$ for Sn^{12+} (figures 12 and 13) and Sn^{13+} (figures 14 and 15). The fractional population of charge state $q+$ in all three cases, $P_{\rm frac}^{q+}$, is $(P_{\rm frac}^{11+}, P_{\rm frac}^{12+}, P_{\rm frac}^{13+})$ = (i) (0.09,0.26,0.36), (ii) (10^{-3},0.01,0.08) and (iii) (10^{-3},0.02,0.17) The following observations are common to all plots:

- Dielectronic capture is the dominant outflux mechanism for the ground-state configuration as well as a few excited configurations. Its dependence on density is generally rather weak.
- The fractional contribution of autoionization to population outflux, $\tilde{\Gamma}_C^{ai}$, is largest for case (iii).
- The fractional contribution of spontaneous emission to population outflux, $\tilde{\Gamma}_C^{se}$, increases with decreasing free-electron density.

We also present the quenching parameter Q_C for Sn^{12+} (figure 16) and Sn^{13+} (figure 17) ions in case (iii). As was the case for Sn^{14+}, the radiative channels associated with $4p-4d$ and $4d-4f$ transitions admit large Q_C values. An additional observation can be made: with increasing ionization, the Q_C values associated with the $4p^54d^{n+1}$ and $4p^44d^{n+2}$ configurations decrease, while those associated with $4p^64d^{n-1}4f$ and $4p^54d^n4f$ configurations increase.

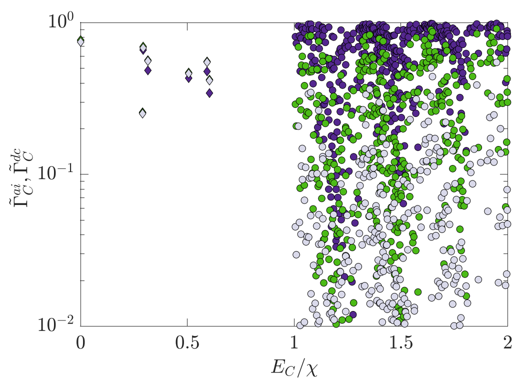

Figure 12. Same as figure 3 but for Sn^{12+}. Our calculations give χ = 256.6 eV.

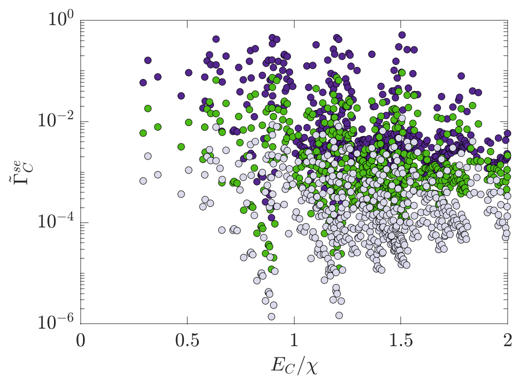

Figure 13. Same as figure 5 but for Sn^{12+}.

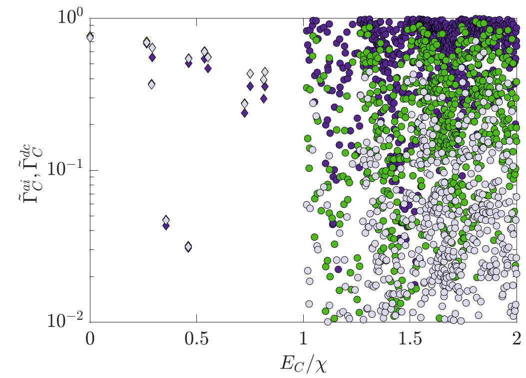

Figure 14. Same as figure 3 but for Sn^{13+}. Our calculations give $\chi = 282.6$ eV.

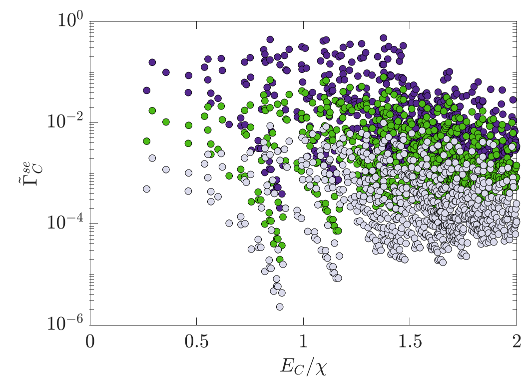

Figure 15. Same as figure 5 but for Sn^{13+}.

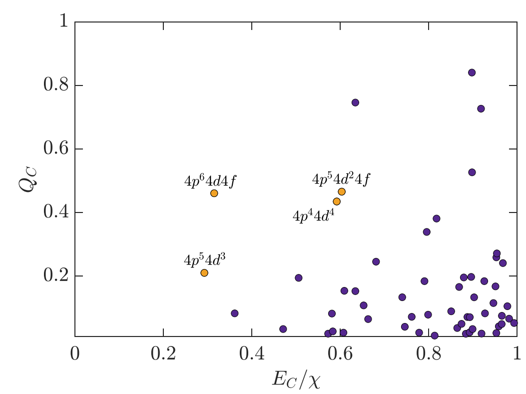

Figure 16. Same as figure 6 but for Sn^{12+}. Our calculations give $\chi = 256.6$ eV.

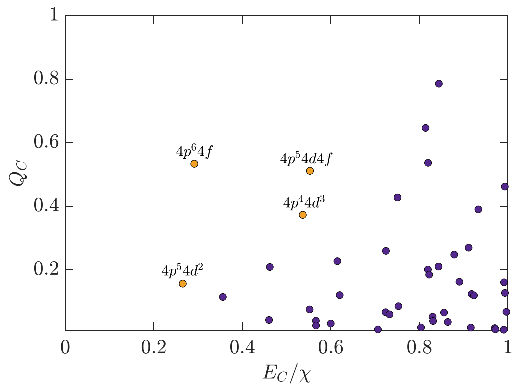

Figure 17. Same as figure 6 but for Sn^{13+}. Our calculations give $\chi = 282.6$ eV.

References

[1] Huebner W F and Barfield W D 2014 *Opacity* (Springer)
[2] Sheil J, Versolato O O, Neukirch A J and Colgan J 2021 *J. Phys. B: At. Mol. Opt. Phys.* **54** 035002
[3] Fontes C J, Colgan J and Abdallah Jr. J 2016 *Modern Methods in Collisional-Radiative Modeling of Plasmas* and Y Ralchenko (Springer) pp 17–50
[4] Torretti F *et al* 2020 *Nat. Commun.* **11** 2334
[5] Bates D R, Kingston A E and Mc Whirter R W P 1962 *Proc. R. Soc.* A **267** 297
[6] Ralchenko Y 2016 *Modern Methods in Collisional-Radiative Modeling of Plasmas* (Springer) (https://doi.org/10.1007/978-3-319-27514-7)
[7] Bauche J, Bauche-Arnoult C and Peyrusse O 2015 *Atomic Properties in Hot Plasmas* (Springer) (https://doi.org/10.1007/978-3-319-18147-9)
[8] Perry T S *et al* 1991 *Phys. Rev. Lett.* **67** 3784
[9] Dozières M *et al* 2015 *High Energy Density Phys.* **17** 231
[10] Bailey J *et al* 2015 *Nature* **517** 56
[11] Nagayama T *et al* 2019 *Phys. Rev. Lett.* **122** 235001
[12] Loisel G P *et al* 2025 *Phys. Rev. Lett.* **134** 095101
[13] Bailey J E *et al* 2025 *Phys. Rev. Lett.* **135** 205101
[14] Iglesias C A and Rogers F J 1996 *Astrophys. J.* **464** 943
[15] Badnell N R, Bautista M A, Butler K, Delahaye F, Mendoza C, Palmeri P, Zeippen C J and Seaton M J 2005 *Mon. Not. R. Astron. Soc.* **360** 458
[16] Blancard C, Cossé P and Faussurier G 2012 *Astrophys. J.* **745** 10
[17] Colgan J, Kilcrease D P, Magee N H, Sherrill M E, Abdallah Jr. J, Hakel P, Fontes C J, Guzik J A and Mussack K A 2016 *Astrophys. J.* **817** 116
[18] Pain J-C, Gilleron F and Comet M 2017 *Atoms* **5** 22
[19] Fomenkov I *et al* 2017 *Adv. Opt. Techn.* **6** 173
[20] Bakshi V 2018 *EUV Lithography,* 2nd edn (SPIE Press) (available at: https://spie.org/publications/book/2305674)
[21] Versolato O O 2019 *Plasma Sources Sci. Technol.* **28** 083001
[22] Scott H A, Harte J A, Foord M E and Woods D T 2022 *Phys. Plasmas* **29** 082703
[23] Scott H, Langer S and Frank Y 2023 *Photon Sources for Lithography and Metrology* ed V Bakshi (SPIE Press) pp 71–110
[24] Purvis M A *et al* 2016 Extreme ultraviolet (EUV) lithography VII *International Society for Optics and Photonics* vol 9776 ed E M Panning (SPIE) p 97760K
[25] Schupp R *et al* 2019 *Phys. Rev. Appl.* **12** 014010
[26] Svendsen W and O'Sullivan G 1994 *Phys. Rev.* A **50** 3710
[27] O'Sullivan G *et al* 2015 *J. Phys. B: At. Mol. Opt. Phys.* **48** 144025
[28] Levels associated with these configurations will mix in a configuration-interaction calculation
[29] Neukirch A J and Colgan J 2023 *High Energy Density Phys.* **46** 101034
[30] Sasaki A 2024 *Appl. Phys. Lett.* **124** 064104
[31] Yan G, Gao C, Hou Y, Jin F, Li Y, Zeng J and Yuan J 2024 *Phys. Plasmas* **31** 093303
[32] Gao Y, Su M, He S, Lu H, Liu X, Wu Y, Cao S, Min Q, Sun D and Dong C 2024 *J. Quant. Spectrosc. Radiat. Transfer* **326** 109120
[33] Botz M 2022 Experimental determination of relative electron collision excitation cross sections of highly charged tin in an EBIT (available at: https://hdl.handle.net/21.11116/0000-000C-FCAC-7) (Accessed 17/01/2025)
[34] de Gaufridy de Dortan F 2007 *J. Phys. B: At. Mol. Opt. Phys.* **40** 599
[35] Kučas S, Karazija R, Jonauskas V and Momkauskaitė A 2009 *J. Phys. B: At. Mol. Opt. Phys.* **42** 205001
[36] Koike F and Fritzsche S 2007 *Radiat. Phys. Chem.* **76** 404
[37] Colgan J, Kilcrease D P, Abdallah J, Sherrill M E, Fontes C J, Hakel P and Armstrong G S J 2017 *High Energy Density Phys.* **23** 133
[38] Sheil J, Versolato O, Bakshi V and Scott H 2023 *Atoms* **11** 130
[39] Busquet M and Cossé P 2000 *J. Quant. Spectrosc. Radiat. Transfer* **65** 101
[40] Bauche J and Bauche-Arnoult C 2000 *J. Phys. B: At. Mol. Opt. Phys.* **33** L283
[41] Fournier K B, Bauche J and Bauche-Arnoult C 2000 *J. Phys. B: At. Mol. Opt. Phys.* **33** 4891
[42] Busquet M 2006 *J. Quant. Spectrosc. Radiat. Transf.* **99** 131
[43] Hansen S, Fournier K, Bauche-Arnoult C, Bauche J and Peyrusse O 2006 *J. Quant. Spectrosc. Radiat. Transfer* **99** 272
[44] Bauche J, Bauche-Arnoult C and Peyrusse O 2006 *J. Quant. Spectrosc. Radiat. Transfer* **99** 55

[45] Busquet M 1993 *Phys. Fluids B* **5** 4191
[46] Abdallah Jr. J, Clark R E H and Cowan R D 1988 Theoretical atomic physics code development Vol. I CATS: cowan atomic structure code, los alamos national laboratory report LA-11436-M (https://doi.org/10.2172/6647245)
[47] Cowan R D 1981 *The Theory of Atomic Structure and Spectra* (University of California Press)
[48] Magee N H, Abdallah J, Colgan J, Hakel P, Kilcrease D P, Mazevet S, Sherrill M, Fontes C J and Zhang H 2004 *AIP Conf. Proc.* vol **730** (AIP) pp 168–79
[49] Hakel P, Sherrill M E, Mazevet S, Abdallah Jr J, Colgan J, Kilcrease D P, Magee N H, Fontes C J and Zhang H L 2006 *J. Quant. Spectrosc. Radiat. Transfer* **99** 265
[50] Clark R E H, Abdallah Jr. J and Mann J B 1991 *Astrophys. J.* **381** 597
[51] Stewart J C and Pyatt K D 1966 *Astrophys. J.* **144** 1203
[52] Scheers J *et al* 2020 *Phys. Rev.* A **101** 062511
[53] Bowen C 2001 *J. Quant. Spectrosc. Radiat. Transfer* **71** 201
[54] van Regemorter H 1962 *Astrophys. J.* **136** 906
[55] Shevelko V P 1997 *Atoms and Their Spectroscopic Proeprties* (Springer) p 149
[56] Mewe R 1972 *Astron. Astrophys.* **20** 215
[57] Holstein T 1947 *Phys. Rev.* **72** 1212
[58] Phillips G, Wark J, Kerr F, Rose S and Lee R 2008 *High Energy Density Phys.* **4** 18
[59] Haines B M *et al* 2022 *Phys. Plasmas* **29** 083901
[60] Scott H 2022 *Source Workshop* (EUV Litho Inc.) (available at: https://euvlitho.com/2022/S45.pdf)
[61] Higashiguchi T, Otsuka T, Yugami N, Jiang W, Endo A, Li B, Kilbane D, Dunne P and O'Sullivan G 2011 *Appl. Phys. Lett.* **99** 191502
[62] Soramoto T, Ogiwara A, Morita H, Jiang W, Sakaue K, Ejima T, O'Sullivan G, Namba S and Higashiguchi T 2024 *Opt. Lett.* **49** 5791
[63] Higashiguchi T *et al* 2013 *Opt. Express* **21** 31837
[64] Wu T *et al* 2016 *J. Phys. B: At. Mol. Opt. Phys.* **49** 035001
[65] Li B, Dunne P, Higashiguchi T, Otsuka T, Yugami N, Jiang W, Endo A and O'Sullivan G 2011 *Appl. Phys. Lett.* **99** 231502
[66] Sugar J and Kaufman V 1982 *Phys. Scr.* **26** 419
[67] Churilov S S, Kildiyarova R R, Ryabtsev A N and Sadovsky S V 2009 *Phys. Scr.* **80** 045303